Nanostructures

DOI: 10.1002/anie.201106652

Reversibly Shape-Shifting Organic Optical Waveguides: Formation of Organic Nanorings, Nanotubes, and Nanosheets**

*Naisa Chandrasekhar and Rajadurai Chandrasekar**

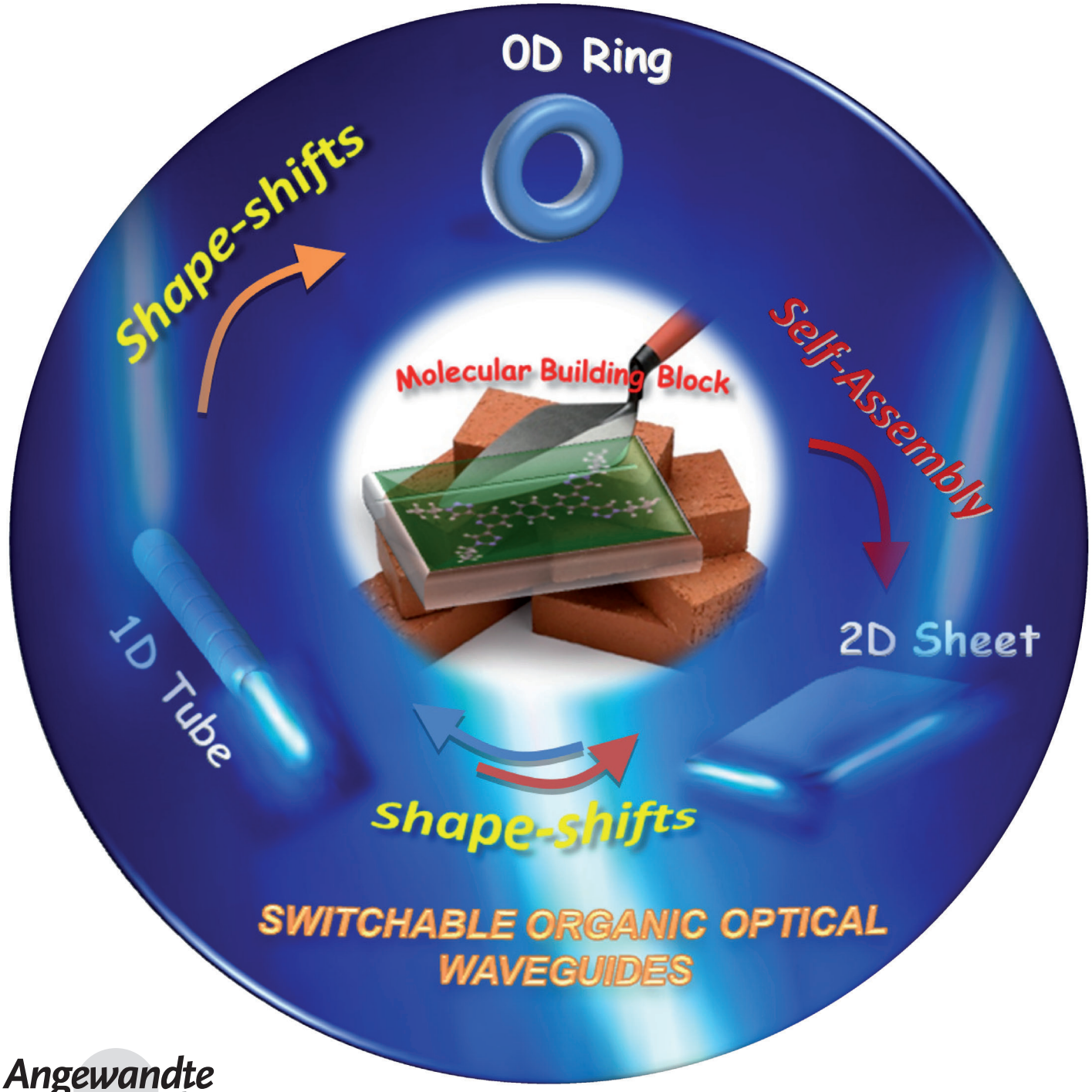

The science of the self-assembly of nano/microstructures from functional, organic, π-conjugated molecules is intriguing because of their potential use in optical, electrical, magnetic, and mechanical nanodevices.[1–4] Recently, tremendous research effort has been aimed at changing the shape of the organic nanosolids by using temperature, stress, photons, ultrasound, and solvents.[2,3] The preparation of shape-shifting nanostructures is emerging as one of the advanced topics in organic-based nanoscience,[2,3] because the functions of the nanoobjects are dependent on their shape and dimensions. In the area of organic nanophotonics in particular, the confinement of optical waves in shape-shifting organic nanostructures is interesting because of their potential use in "smart" nanooptical devices, such as optical waveguides, photonic detectors, and optical sensors.

Until now, no methods for the fabrication of reversibly shape-shifting organic nanostructures that have dimensionally dependent optical waveguiding properties have been available. Most of the reported organic waveguides have defined shapes[5] and, hence, the direction of optical transmission cannot be manipulated. With the aim of fabricating organic optical waveguides that shape-shift reversibly, the roles of the solvents, ultrasound, and the time required for the structural evolution were all effectively controlled and used for the complete growth and isolation of organic nanosolids that have three different dimensions (2D nanosheet, 1D nanotube, and 0D nanoring). Interestingly, the shape-shifting between the 2D nanosheet and the 1D nanotube is reversible and, consequently, so is the direction of optical wave guiding.

Herein, we report an original, bottom-up approach for the preparation of 2D nanosheets, 1D nanotubes, and 0D nanorings by using a solvent- and ultrasound-assisted shape-shifting strategy (0D←1D↔2D). Organic, rhombus-shaped nanosheets were fabricated by the self-assembly of 1,4-bis(1,2′:6′,1″-bis(3-butyl-1*H*-3,4,5-triazolyl)pyridin-4′-yl)benzene (**1**, Figure 1a) in CH_3CN. The shape of the nanosheets was then switched into nanotubes in the presence of water by a rolling mechanism. Ultrasonication of the nanotubes induced the transformation of the nanotubes back into nanosheets, which then reverted back to nanotubes after one day in solution. The nanorings were then formed from the nanotubes after one week in solution by a bending and coiling mechanism. The nanostructures and the mechanisms of formation were characterized by using electron microscopy (SEM, field emission scanning electron microscopy (FESEM), and TEM), selected area electron diffraction (SAED), AFM, and micro-Raman spectroscopy/imaging. The switchable optical waveguiding properties of the nanotube and the nanosheet were investigated by using confocal optical microscopy (Figure 1b).

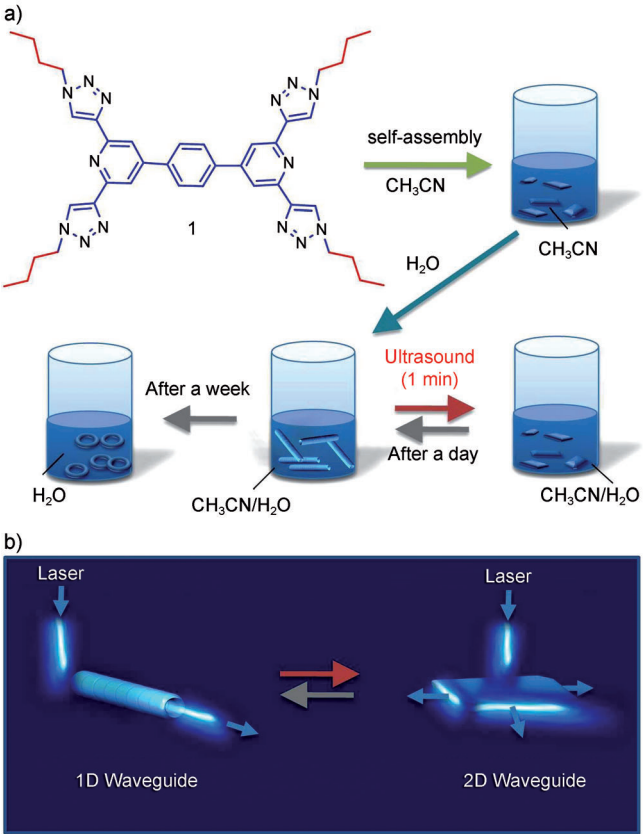

Figure 1. Top: Formation of organic 2D nanosheets, 1D nanotubes, and 0D nanorings from **1** under different self-assembly conditions. Bottom: Reversible optical waveguiding properties of nanosheets and nanotubes.

The building block molecule **1** was synthesized as previously described.[6] Examination of the X-ray structure that was obtained from the sheetlike single crystals of **1** (monoclinic; $P2_1/c$) showed that **1** has unique structural features for hierarchical supramolecular self-assembly. Compound **1** has a nearly planar, rod-shaped arrangement of three aromatic rings as the central segment ($N_{py}\cdots N_{py}$ distance = 1.13 nm) and four triazole rings with butyl chains attached to the four corners of the rigid segment. Furthermore, the triazole ring nitrogen atom (N2) participates in two C–H···N intermolecular hydrogen-bonding interactions with the phenyl ring protons [N2···H4 = 2.737 Å; N2···H5 = 2.635 Å] that play a vital role in the supramolecular ordering and self-assembly. Through these intermolecular forces, molecules of **1** aggregate and form a 1D sheetlike structure with a thickness of 1.76 nm in the crystallographic *b*,*c* plane (Figure 2b). Every molecular-level layer is tightly packed along the crystallographic *a* axis with interpenetrating alkyl chains, and these layers form stacked, sheetlike, supramolecular aggregates of **1** (Figure 2a,c).

[*] N. Chandrasekhar, Prof. Dr. R. Chandrasekar
Functional Molecular Micro/Nanostructures Laboratory, School of Chemistry, University of Hyderabad (UoH)
Prof. C. R. Rao Road, Gachi Bowli, Hyderabad 500 046 (India)
E-mail: rcsc@uohyd.ernet.in
chandrasekar100@yahoo.com
Homepage: http://sites.google.com/site/rajaduraichandrasekargroup/

[**] This work was financially supported by DST (no. SR/FTP/CS-115/2007). We thank the Centre for Nanotechnology (CFN), UoH for providing the TEM facility and M. Durga Prasad for recording the TEM Micrographs. N.C. thanks CSIR-New Delhi for a SRF.

Supporting information for this article is available on the WWW under http://dx.doi.org/10.1002/anie.201106652.

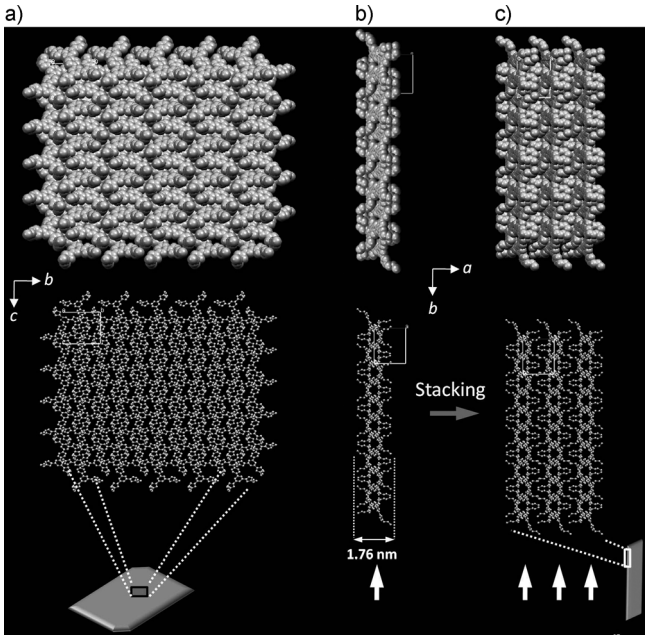

Figure 2. Possible formation mechanism of 2D sheetlike aggregates from molecular sheets. a) Top view of the single-crystal X-ray packing diagram of **1** along the crystallographic *a* axis. b) Side view of a 1.76 nm molecular-level sheet along the crystallographic *c* axis. c) Side view of layer-by-layer aggregation of molecular-level sheets along the crystallographic *a* axis.

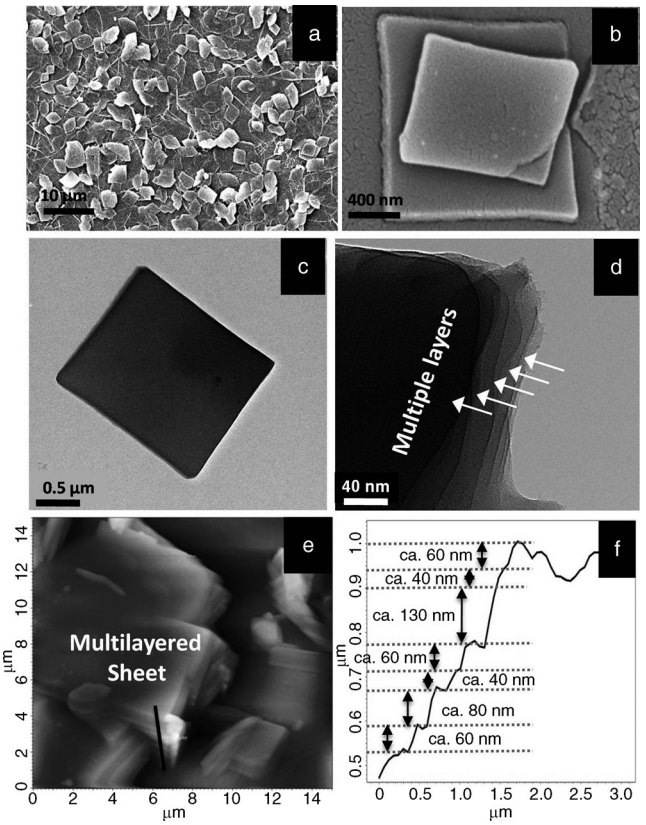

Figure 3. Electron micrographs of rhombus-shaped nanosheets made from **1**: a) SEM image of randomly distributed sheets. b) FESEM image of a nanosheet on top of another nanosheet. Bright-field TEM images: c) A single nanosheet with dark contrast. d) A closer view of the TEM image of the multilayered edges of a nanosheet. e) Non-contact-mode AFM image of a layered nanosheet. f) Thickness profile of the stacked thin layers of the nanosheet shown in image (e).

A solution of **1** (1 mg) in CH_3CN (2 mL) was used to grow the nanostructures. Two drops of the solution was slowly evaporated on a clean glass surface at room temperature or the solution was directly deposited on a carbon-coated TEM grid for electron microscopy analysis. Examination of an as-prepared sample of the nanostructures by SEM showed that rhombus-shaped 2D nanosheets were formed (Figures 3a,b). Investigation of a single nanosheet by TEM showed an area of dark contrast relative to the bulk area of the nanosheets (Figure 3c), and various levels of contrast at the sheet edges (Figure 3d). A closer examination of a nanosheet edge confirmed the presence of several thin organic layers, which have thickness-dependent contrasts and are stacked together to form the multilayered bulk nanosheet (Figures 3c,d). Noncontact-mode AFM images of the bulk nanosheets showed that the thickness of the nanosheet is in the range of approximately 200 nm to 500 nm. An AFM height profile of a multilayered sheet edge showed that the thickness of each individual layer is in the range of approximately 40 nm to 130 nm (Figures 3e,f).

To determine the number of molecular-level layers that make up the individual layers in the nanosheet, and their orientation in the nanosheet, comparative micro-Raman imaging/spectroscopy was performed on the nanosheets and the sheetlike bulk crystals of **1** (Figure S3 in the Supporting Information). The molecular-level layers have a thickness of approximately 1.76 nm (Figure 2b). Interestingly, both samples have similar Raman shifts and comparable intensity patterns as a result of the existence of identical polarizability that is caused by the similar molecular orientation. These results suggested that the single-crystal X-ray packing structure could be used to determine the number of molecular-level layers in each of the individual layers. Comparison of the X-ray and AFM data showed that each approximately 40 nm thick single layer is composed of approximately 23 molecular-level layers ($23 \times 1.76\ \text{nm} = 40\ \text{nm}$).

Interestingly, upon the addition of high purity water (1 mL), the nanosheets transformed into nanotubes after one day in solution, as shown by SEM images (Figure 4). FESEM and TEM studies showed that the tubes have open ends (Figure 4b,c). Furthermore, the AFM profile measurements of a nanotube were approximately $1.5\ \mu\text{m} \times 200\ \text{nm} \times 100\ \text{nm}$ (length × diameter × height, Figures 4e,f). In some areas of the sample a few rolled nanotubes were found along with the nanosheets (Figure S1a–c in the Supporting Information), which suggests that the nanotubes are formed from nanosheets through a rolling mechanism. A closer examination of a tube clearly showed the presence of a sheet edge, which is formed during the sheet rolling process (Figure S1c in the Supporting Information). The nanotubes changed back into nanosheets when ultrasound was applied for one minute to the solution of the nanotubes. These nanosheets again reverted back to the low-energy tubular shape after one day in solution.

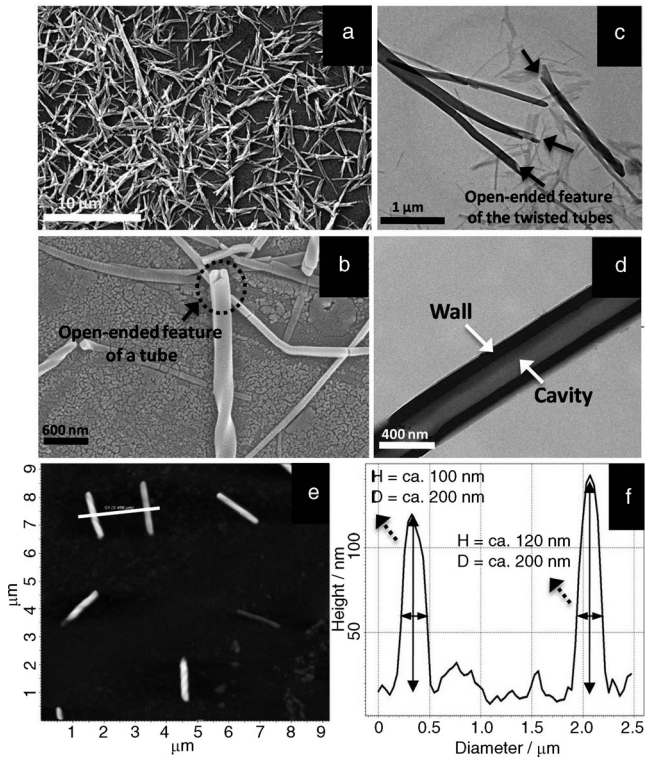

Figure 4. Electron micrographs of nanotubes made from **1**: a) SEM image of randomly distributed, twisted nanotubes. b) FESEM image of a single nanotube with a helical twist. The black dotted circle indicates the open end of the tube. Bright-field TEM images: c) Nanotubes with irregular open ends. d) A single tube with different contrasts from the wall and cavity. e) Noncontact-mode AFM image of the nanotubes. f) Height and diameter profiles of the nanotubes shown in image (e).

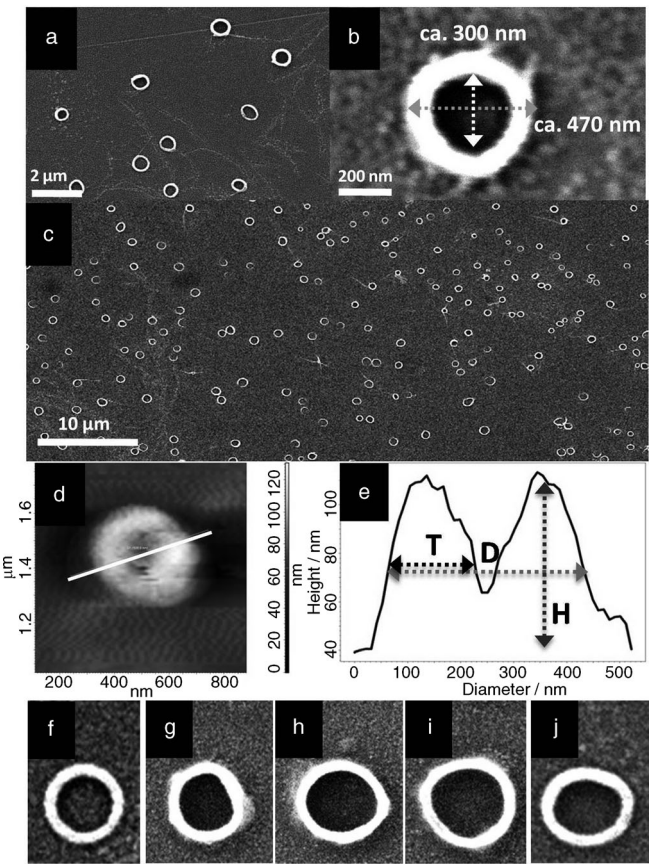

Figure 5. a) SEM image of nanorings made from **1**. b) A closer view of a nanoring. c) Larger surface area coverage of nanorings. e) AFM height, thickness, and diameter profiles of the ring shown in image (d). f)–j) Some representative rings.

Analysis of the solution that contained the nanotubes after a week by electron microscopy revealed a complete transformation of the nanotubes into thermodynamically more-stable nanorings (Figure 5). Analysis of a single ring by SEM showed that it was nearly circular with outer and inner diameters of approximately 450 nm and 300 nm, respectively. Furthermore, AFM topography of a single ring showed that the outer diameter, height, and thickness were approximately 370 nm, 60 nm, and 170 nm, respectively (Figures 5 d,e). The thickness of the ring (t) suggests that it was formed from a tube of comparable diameter. Intriguingly, the overall surface area coverage of the rings is greater than 100 μm^2.

The driving force behind the 2D→1D→0D shape transformations is probably different molecular-level forces, which are assisted by the solvent(s). Recently, Desiraju and coworkers have demonstrated the correlation between the intermolecular packing and crystal deformation directions in organic single crystals by applying external stress.[7] In the present case, the occurrence of the shape-shifts in the absence of any external load suggests that the critical activation energy (critical strain) that is needed to overcome the intermolecular binding forces is very low. The driving force behind the structural deformation probably originates from the "hydrophobic surface effect" of the organic nanostructures in the presence of water, which forces the structures to curve to reduce their exposure to water (Figure 6). Analysis of the single-crystal X-ray structure of **1** showed that the molecular-level sheets are stacked along the crystallographic *b*,*c* plane (Figure 2). Thus, the movement of the molecular-level sheets along the crystallographic *a* axis is not possible because of the higher activation energy. Hence, the low-energy sliding motion of the individual molecular-level sheets along the crystallographic *b*,*c* plane is probably involved in the deformation process. Furthermore, the micro-Raman and selected area electron diffraction (SAED) data for the nanosheets, nanotubes, and nanorings clearly demonstrated that indeed the three organic nanosolids have three different molecular packing arrangements, which are a result of the solid-state molecular movements during the deformation process (see Figures S3 and S4 in the Supporting Information).

To explore the mechanistic transformation of the nanotubes into nanorings, the solution that contained the nanotubes was analyzed at different intervals to isolate the intermediates. Data from FESEM and AFM experiments showed that the formation mechanism of a nanoring is a very complex process (Figure 6 and Figures S1 and S2 in the Supporting Information), but it can be explained by using a simple continuous elastic model.[8] The ring formation process consists of a dimensional collapse, that is, coiling of the nanotube to form an intermediate, looplike structure. The

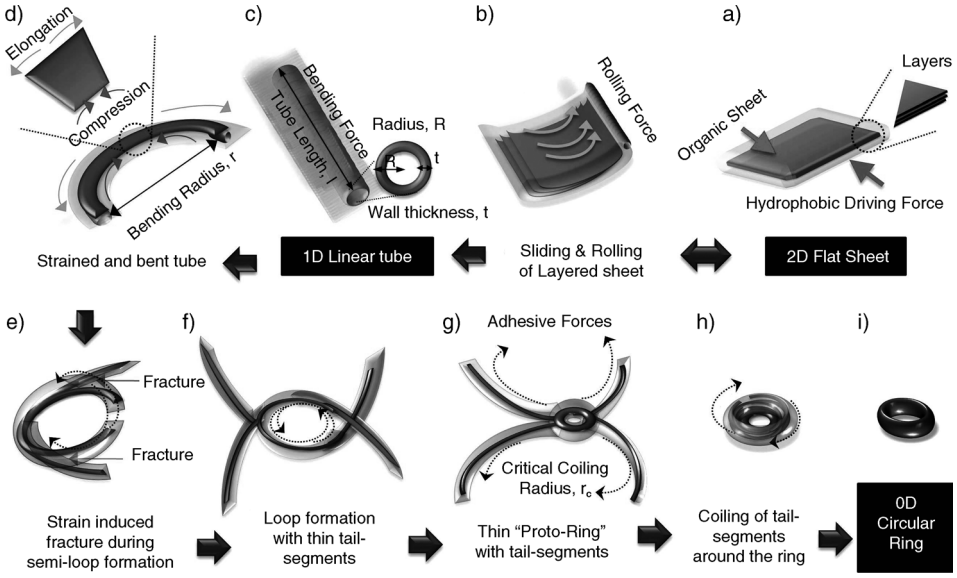

Figure 6. Representation of the solid-state shape-transformation (2D→1D→0D) mechanism that is driven by the hydrophobic forces, and the resulting nanostructures. The schematic diagrams are based on electron microscopy and AFM data (see Figures S1 and S2 in the Supporting Information).

formation of the loop probably gives new stabilization pathways through intermolecular noncovalent interactions. Opposing this loop-stabilizing energy, the bending process imparts strain energy (E_S) on the nanotube because of the bending-induced curvature formation, which is a result of collective translational molecular motions in the solid state. The magnitude of E_S increases with decreasing coiling radius r. From continuum mechanics[9] $E_S = (YI)\,l/2\,r^2$, where Y is the Young modulus, l is the tube length, r is the loop radius, and $I = (\pi/4)[R^4-(R-t)^4]$ is the geometrical moment of inertia of a tube with an external radius R and a wall thickness t.

Furthermore, the bending of a tube exerts elongation and compressive forces on the outer and inner part of the curved structure, respectively (Figure 6d). In other words the translational motions of the molecules are in opposite directions in the outer and inner part of the curved, dynamic solid structure. When the coiling radius decreases further because of the build-up of strain energy, fracture occurs along the axis of the tube (thereby reducing the solid-state packing energy) and a semiloop structure with two tail-like tube segments is formed (Figure 6e). At this stage, the tubular morphology collapses. The formation of a circular loop involves energy, that is, the minimum r that is necessary for complete loop formation further increases the strain energy, thereby causing additional fractures, and four tails segments around a loop are formed (Figure 6f). The interactions of the tail segments of the tube with the loop again involve noncovalent binding energy, which increases with the coiling of the leftover tail segments around the thin protoring, and finally a circular nanoring is formed (Figures 6g,h). The formation of nanorings of different diameters (approximately 400 nm) suggests that the critical r_c (Figure 6g) depends on the length and the thickness of the nanotubes. To induce these energetically complex solid-state deformations, both positive and negative entropy contributions must also play an important role during the deformation process around the surface of the tube as a result of the immediate aqueous environment.[9] The evaporation of acetonitrile increases the "repulsive" hydrophobic effect between the water molecules and the tubes, and the entropy increases ($+\Delta S$), because of the constraint imposed on the water molecules to form hydrogen bonds near the tube surface–water interface. Coiling of the bulk of the tubes is entropically more favored ($+\Delta S$), although it decreases ΔS slightly at the interface by decreasing the water–tube contact area.

The optical waveguiding properties of the nanosheets and the nanotubes were examined by using a laser confocal microscopy coupled with a color eyepiece video camera. The images were collected through a 488 nm long-pass edge filter (Figure 7). As a result of the reversible shape-shifting character of the nanosolids, it was

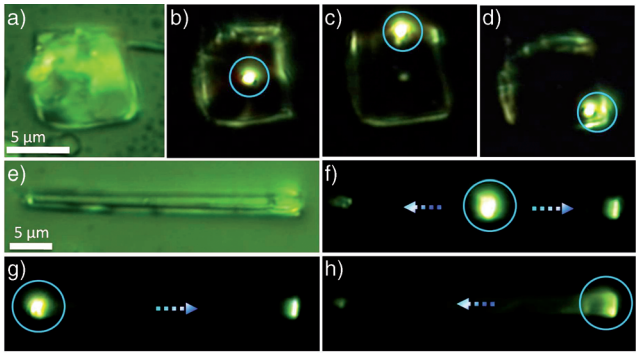

Figure 7. Confocal laser microscopy images collected through a 488 nm long-pass edge filter: a)–d) A 2D nanosheet. e)–h) A 1D nanotube. a) Bright-field image of a nanosheet. Position of the laser beam input: b) at the center; c) at the edge; d) at the corner. e) Bright-field image of a nanotube. Position of the laser beam input: f) at the center; g) at the left end; h) at the right end. The dotted arrows show the direction of light propagation.

hypothesized that the directions of optical confinement could also be switched. It was anticipated that the tubular and layered geometries could facilitate the propagation of light in 1D and 2D, respectively. For the waveguiding experiments, the output of the Ar laser beam (488 nm) was directly focused on the sample. Since **1** does not have any absorption in the 488 nm region, no molecular excitation (hence, no absorption and fluorescence) as a result of the laser energy was expected. When the laser beam was focused orthogonally at the center of the plane of a 2D sheet, propagation of laser light in all the four directions of the sheet was observed (Figure 7b).

Focusing the laser beam at one of the edges showed that the sheet guided the light mostly towards the opposite edge (Figure 7c). Interestingly, illumination the corner of the sheet with the laser beam resulted in light propagation to the two diagonal edges (Figure 7d). These results confirmed that the nanosheets acted as a waveguide in 2 dimensions, and that the direction of propagation of the light was dependant on the path of the light input. Furthermore, when the laser light was focused at the center of a 1D tube, propagation of the light to both open ends of the tube was observed (Figure 7f). Pointing the laser beam at the left and right side of the tube resulted in the propagation of light in the opposite exit directions (Figure 7g and h), which confirmed the 1D optical waveguiding nature of the tube. These experiments clearly demonstrated the possibility of switching the wave guiding direction to either 1 or 2 dimensions by changing the tubes to sheets and vice versa.

In conclusion, both solvent and ultrasound can be used to induce mechanical deformation (shape-shifting) in organic solids to access organic solids that have three different dimensions (2, 1, and 0 dimensions) at appropriate time intervals. The detailed mechanistic transformation studies showed that the hydrophobic surface energy is the main driving force behind the plastic deformation of the solids. Furthermore, exploiting the reversible shape-shifting nature of both nanosheets and nanotubes, switching of the light propagation (optical waveguiding) direction in 1 and 2 dimensions was demonstrated. This "bottom-up" method is a useful technique for generating directionally switchable organic optical waveguides.

Received: September 19, 2011
Revised: December 12, 2011
Published online: January 17, 2012

Keywords: nanostructures · nanotubes · self-assembly · shape-shifting · waveguides

[1] a) M. R. Ghadiri, J. R. Granja, R. A. Milligan, D. E. McRee, N. Khazanovich, *Nature* **1993**, *366*, 324; b) L. Brunsveld, B. J. B. Folmer, E. W. Meijer, R. P. Sijbesma, *Chem. Rev.* **2001**, *101*, 4071; c) S. Prasanthkumar, A. Saeki, S. Seki, A. Ajayaghosh, *J. Am. Chem. Soc.* **2010**, *132*, 8866; d) S. Prasanthkumar, A. Gopal, A. Ajayaghosh, *J. Am. Chem. Soc.* **2010**, *132*, 13206; e) A. Ajayaghosh, V. K. Praveen, C. Vijayakumar, *Chem. Soc. Rev.* **2008**, *37*, 109; f) Y. Hirai, S. S. Babu, V. K. Praveen, T. Yasuda, A. Ajayaghosh, T. Kato, *Adv. Mater.* **2009**, *21*, 4029; g) M. Urdampilleta, S. Klyatskaya, J.-P. Cleuziou, M. Ruben, W. Wernsdorfer, *Nat. Mater.* **2011**, *10*, 502; h) A. Candini, S. Klyatskaya, M. Ruben, W. Wernsdorfer, M. Affronte, *Nano Lett.* **2011**, *11*, 2634.

[2] a) H. Shao, J. R. Parquette, *Angew. Chem.* **2009**, *121*, 2563; *Angew. Chem. Int. Ed.* **2009**, *48*, 2525; b) Y. Lim, K.-S. Moon, M. Lee, *Chem. Soc. Rev.* **2009**, *38*, 925; c) H. J. Kim, T. Kim, M. Lee, *Acc. Chem. Res.* **2011**, *44*, 72; d) J. W. Ciszek, L. Huang, Y. Wang, C. A. Mirkin, *Small* **2008**, *4*, 206; e) T. D. Nguyen, S. C. Glotzer, *Small* **2009**, *5*, 2092; f) E. Lee, Z. Huang, J.-H. Ryu, M. Lee, *Chem. Eur. J.* **2008**, *14*, 6957; g) D. Kühne, F. Klappenberger, W. Krenner, S. Klyatskaya, M. Ruben, J. V. Barth, *Proc. Natl. Acad. Sci. USA* **2010**, *107*, 21332; h) S. Yang, X. Feng, X. Wang, K. Müllen, *Angew. Chem.* **2011**, *123*, 5451; *Angew. Chem. Int. Ed.* **2011**, *50*, 5339; i) S. Yagai, S. Mahesh, Y. Kikkawa, K. Unoike, T. Karatsu, A. Kitamura, A. Ajayaghosh, *Angew. Chem.* **2008**, *120*, 4769; *Angew. Chem. Int. Ed.* **2008**, *47*, 4691.

[3] a) A. Ajayaghosh, V. K. Praveen, *Acc. Chem. Res.* **2007**, *40*, 644; b) A. Ajayaghosh, P. Chithra, R. Varghese, *Angew. Chem.* **2007**, *119*, 234; *Angew. Chem. Int. Ed.* **2007**, *46*, 230; c) T. Nakanishi, W. Schmitt, T. Michinobu, D. G. Kurth, K. Ariga, *Chem. Commun.* **2005**, 5982; d) M. Sathish, K. Miyazawa, J. P. Hill, K. Ariga, *J. Am. Chem. Soc.* **2009**, *131*, 6372; e) S. Yagai, S. Kubota, H. Saito, K. Unoike, T. Karatsu, A. Kitamura, A. Ajayaghosh, M. Kanesato, Y. Kikkawa, *J. Am. Chem. Soc.* **2009**, *131*, 5408; f) D. Ke, C. Zhan, A. D. Q. Li, J. Yao, *Angew. Chem.* **2011**, *123*, 3799; *Angew. Chem. Int. Ed.* **2011**, *50*, 3715.

[4] a) N. Chandrasekhar, R. Chandrasekar, *Chem. Commun.* **2010**, *46*, 2915; b) S. Basak, R. Chandrasekar, *Adv. Funct. Mater.* **2011**, *21*, 667; c) Y. S. L. V. Narayana, R. Chandrasekar, *ChemPhysChem* **2011**, *12*, 2391.

[5] a) F. Balzer, V. G. Bordo, A. C. Simonsen, H.-G. Rubahn, *Phys. Rev. B* **2003**, *67*, 115408; b) Y. S. Zhao, H. Fu, A. Peng, Y. Ma, Q. Liao, J. Yao, *Acc. Chem. Res.* **2010**, *43*, 409; c) K. Takazawa, Y. Kitahama, Y. Kimura, G. Kido, *Nano Lett.* **2005**, *5*, 1293; d) H. Yanagi, T. Morikawa, *Appl. Phys. Lett.* **1999**, *75*, 187; e) Y. S. Zhao, J. J. Xu, A. D. Peng, H. B. Fu, Y. Ma, L. Jiang, J. N. Yao, *Angew. Chem.* **2008**, *120*, 7411; *Angew. Chem. Int. Ed.* **2008**, *47*, 7301.

[6] N. Chandrasekhar, R. Chandrasekar, *J. Org. Chem.* **2010**, *75*, 4852.

[7] a) C. M. Reddy, R. C. Gundakaram, S. Basavoju, M. T. Kirchner, K. A. Padmanabhan, G. R. Desiraju, *Chem. Commun.* **2005**, 3945; b) C. M. Reddy, M. T. Kirchner, R. C. Gundakaram, K. A. Padmanabhan, G. R. Desiraju, *Chem. Eur. J.* **2006**, *12*, 2222.

[8] a) B. I. Yakobson, C. J. Brabec, J. Bernholc, *Phys. Rev. Lett.* **1996**, *76*, 2511; b) R. Martel, H. R. Shea, P. Avouris, *J. Phys. Chem. B* **1999**, *103*, 7551.

[9] a) D. J. Barber, R. Loudon, *An Introduction to the Properties of Condensed Matter*, Cambridge University Press, Cambridge, **1989**; b) C. Tanford, *The Hydrophobic Effect*, Wiley, New York, **1980**.

